Laser Guide Star for Large Segmented-aperture Space Telescopes. I. Implications for Terrestrial Exoplanet Detection and Observatory Stability

The Astronomical Journal, 157:36 (12pp), 2019 January https://doi.org/10.3847/1538-3881/aaf385

Laser Guide Star for Large Segmented-aperture Space Telescopes. I. Implications for Terrestrial Exoplanet Detection and Observatory Stability

E. S. Douglas[1], J. R. Males[2], J. Clark[1], O. Guyon[2], J. Lumbres[2], W. Marlow[1], and K. L. Cahoy[1,3]
[1] Department of Aeronautics and Astronautics, Massachusetts Institute of Technology, 77 Massachusetts Avenue, Cambridge, MA 02139, USA
[2] Steward Observatory, University of Arizona, 933 N Cherry Avenue, Tucson, AZ 85721, USA
[3] Department of Earth, Atmospheric, and Planetary Science, Massachusetts Institute of Technology, 77 Massachusetts Avenue, Cambridge, MA 02139, USA
Received 2018 August 29; revised 2018 November 13; accepted 2018 November 20; published 2019 January 4

Abstract

Precision wavefront control on future segmented-aperture space telescopes presents significant challenges, particularly in the context of high-contrast exoplanet direct imaging. We present a new wavefront control architecture that translates the ground-based artificial guide star concept to space with a laser source on board a second spacecraft, formation flying within the telescope's field of view. We describe the motivating problem of mirror segment motion and develop wavefront sensing requirements as a function of guide star magnitude and segment motion power spectrum. Several sample cases with different values for transmitter power, pointing jitter, and wavelength are presented to illustrate the advantages and challenges of having a non-stellar-magnitude noise limited wavefront sensor for space telescopes. These notional designs allow increased control authority, potentially relaxing spacecraft stability requirements by two orders of magnitude and increasing terrestrial exoplanet discovery space by allowing high-contrast observations of stars of arbitrary brightness.

Key words: instrumentation: adaptive optics – instrumentation: high angular resolution – planets and satellites: detection – space vehicles: instruments – telescopes

1. Introduction

Reflected light imaging of terrestrial exoplanets with space telescopes requires both large apertures and extreme instrument stability. The brightest observed flux ratio (ζ_c; Table 1) between a planet with an Earth-like albedo and radius and a Sunlike host star is approximately 10^{-10} or 25 magnitudes, with deeper contrasts at intermediate phases and spectral absorption features (Woolf et al. 2002; Turnbull et al. 2006; Robinson et al. 2011). As an alternative to coronagraphs, formation flying large (>40 m) external occulters, or starshades, provide high sensitivity in exchange for long wait times between targets to reposition the occulter. Given this high overhead, starshades may be preferable for spectroscopy of known exoplanets, while coronagraphs may provide higher yields in blind searches (Stark et al. 2016a). In order to discover and/or characterize a significant number of Earth-like planets in a survey of nearby stars within a typical five-year mission lifetime, apertures greater than 4 m in diameter and coronagraphic attenuation of starlight (i.e., contrast) to below 10^{-11} are likely needed (Stark et al. 2014, 2016b).

Stark et al. (2015) modeled detection limits for habitable-zone Earth-like exoplanets with a 10 m space observatory for a total mission exposure time of 1 yr (including spectral characterization). By holding other model assumptions constant, they found a power-law dependence of yield on contrast of $\zeta_C^{-0.1}$. In the Stark et al. (2015) example case, decreasing the contrast from 10^{-10} to 10^{-9} decreases the mission yield from 26 to 14 Earth-like planets. Our understanding of what constitutes habitability is still severely limited (Seager 2013), and a near doubling of the number of habitable-zone planets observed will have a profound effect on our understanding of the diversity of chemistry and conditions on Earthlike planets, which underscores the importance of maximizing contrast.

Internal coronagraphic instruments that attenuate starlight and allow exoplanet detection at small separations are highly sensitive to wavefront errors (see Serabyn 2000; Traub & Oppenheimer 2010). The wavefront must be sufficiently stable in order to sense, control, and subtract systematic leakage (commonly known as "speckles," see Racine et al. 1999; Perrin et al. 2003). In order to maximize collecting area and resolution, large apertures (4–15 m) are also needed. To achieve such large apertures, missions such as the proposed Large UV/Optical/Infrared Surveyor (LUVOIR) concept, are expected to use primary mirrors made up of multiple meter-scale segments (Eisenhower et al. 2015).

Segment motion is a mid-spatial frequency wavefront error that causes speckles inside a coronagraph dark hole (Ruane et al. 2017; Leboulleux et al. 2018). Thus, the wavefront error in the segment tip, tilt, and piston modes must be highly stabilized for imaging and spectroscopy of Earth-like exoplanets in visible light. A variety of efforts are underway to develop and test coronagraphs for segmented apertures (Miller et al. 2015; N'Diaye et al. 2016; Ruane et al. 2017; Hicks et al. 2018; Martinez et al. 2018). Root-mean-squared (rms) Wavefront Error (WFE) stabilities below 10 picometers are commonly specified to reach the required flux ratios (Lyon & Clampin 2012; Bolcar 2017). As discussed in Section 2.3, the particular WFE requirements depend on the temporal power spectral density (PSD) of the segment motion.

Observatories on the ground have demonstrated alignment of telescopes made up of multiple segments. For example, the Multiple Mirror Telescope (Beckers et al. 1982) alignment is achieved by actively controlling a segmented secondary mirror, while for the W.M. Keck telescope, alignment is achieved by controlling primary segment position (Jared et al. 1990). Similar systems are planned for nanometer level control of upcoming 30 m class telescope segments (Macintosh et al. 2006; Gonte et al. 2008; Troy et al. 2008; Bouchez et al. 2012).

Different means of sensing segment motion to picometer levels have been proposed: edge sensors, wavefront sensing using the target star, or internal metrology (Feinberg et al.

Table 1
Table of Symbols

Symbol	Unit	Description
ζ_c		planet–star flux ratio
f	[Hz]	disturbance frequency
α		power-law index of the disturbance PSD
σ_{10}	[pm]	1σ stability over 10 minutes
f_s	[Hz]	sampling frequency
$\sigma_{\rm ron}$	[electrons]	detector readout noise
$\tau_{\rm wfs}$	[s]	wavefront sensor exposure time
T_0	minutes	inverse of the disturbance PSD knee frequency
θ	radian	transmitter half-angle divergence
T_p	ratio	system throughput and QE
x_0	[radian]	pointing error
x	[radian]	radial displacement from Gaussian beam
w	[radian]	Gaussian beamwidth
MFD	[um]	mode-field diameter
w_0	[m]	beam waist
$\lambda_{\rm WFS}$	[nm]	wavefront sensing wavelength

2017). Wavefront sensing using target starlight minimizes calibration errors between sensors and the science image; however, photon noise limits wavefront sensing (and science observations) to bright nearby stars (Lyon & Clampin 2012; Stahl et al. 2013, 2015). Contrast depends on wavefront sensing and control, which in turn requires sufficient flux for effective wavefront sensing. A guide star of arbitrary brightness offers the potential to significantly increase the yield of a survey, by increasing the sensitivity of a given observatory to exoplanets even for dim targets and can significantly increase yield for large aperture space telescopes.

We present a new approach to wavefront sensing, employing a bright formation flying calibration source, serving as an artificial guide star and enabling high-cadence segment control during coronagraph observations of stellar systems regardless of host star magnitude.

Artificial guide stars were developed for ground-based astronomical telescopes several decades ago. Foy & Labeyrie (1985) proposed using laser light from the ground to illuminate a bright artificial star at high altitudes as a reference for ground-based adaptive optics systems. This was soon demonstrated by exciting mesospheric sodium (Thompson & Gardner 1987), an approach that became a widely used means of improving adaptive optics performance (e.g., Max et al. 1997; Wizinowich et al. 2006; Holzlöhner et al. 2010).

Several authors have considered a space-borne laser guide star (LGS) for use with ground-based telescopes, which would provide a diffraction-limited point source and operate at lower power than atmospheric backscatter guide stars. Greenaway & Smith (1990) proposed a laser source in cis-lunar orbit for observing low-decl. astronomical targets. Similarly, drones have been proposed as platforms for downward looking laser guide stars (Basden et al. 2018). Marlow et al. (2017) proposed a CubeSat nanosatellite in geosynchronous orbit for astronomical imaging and space situational awareness from the ground.

Adaptive optics systems for use with ground-based telescopes primarily mitigate aberrations caused by atmospheric turbulence. This is different from the motivation for a space-based laser guide star paired with a large aperture segmented space telescope. Instead of atmospheric turbulence, a space-based laser guide star enables correction of static and dynamic wavefront errors caused by onboard structural, thermal, and optical sources. Building on the concept of a CubeSat LGS described by Marlow et al. (2017), this work explores the adaptation of a small LGS spacecraft to enable precise wavefront sensing of a large segmented-aperture space telescope. While spacecraft formation flight is challenging, two-spacecraft precision formation flight without use of the Global Positioning System for navigation has been demonstrated by the Gravity Recovery and Interior Laboratory mission in lunar orbit with $\sim 1\ \mu{\rm m\ s}^{-1}$ accuracy (Smith & Zuber 2016) and it may be a viable solution for missions of the size and complexity of LUVOIR. Section 2 describes basic parameters of a laser guide star spacecraft, the problem of segment motion in the context of high-contrast imaging, and develops a notional wavefront sensor (WFS). Section 4 presents a laser guide start mission architecture to meet the performance requirements of a large segmented-aperture telescope mission. Section 5 discusses the science impact of maintaining contrast while observing dim target stars and the engineering impact of relaxing telescope stability requirements. Section 6 provides a summary of the benefits of a laser guide star system, and discusses ongoing experiments and next steps toward developing a laser guide star technology demonstration.

2. Methods: Establishing Telescope Stability Requirements for Earth-like Planet Detection

Large aperture space telescope designs call for deployed segmented apertures in order to fit within launch vehicle fairings (e.g., Postman et al. 2009; Stahl & MSFC Advanced Concept Office 2016). A low-mass segmented telescope is easier to launch, package, and maneuver; while a stiffer, more massive telescope is easier to align and stabilize against disturbances. Segment motion arises primarily from vibrations in the spacecraft, due to imperfections in reaction wheel bearings and balance, or variations in thruster performance (Mier-Hicks & Lozano 2017), which are transmitted by the relatively flexible, low-mass spacecraft structure (Bronowicki 2006). Stahl et al. (2015) find that a 0.25 minute wavefront sensing cadence is required for a 12 m telescope observing a $m_{\rm V} = 5$ star, with a stability 10 times longer ($\gtrsim$2.5 minutes) to ensure control system performance (see also Lyon & Clampin 2012; Stahl et al. 2013). Depending on the coronagraph, the wavefront error requirement can be significantly relaxed for lower spatial order modes, such as global tilt or focus (Ruane et al. 2017). However, segment motion primarily contributes at higher spatial frequencies, degrading contrast at planet–star separations of significant interest.

2.1. Impact of Wavefront Error on Coronagraph Contrast

Modeling of exoplanet yield versus contrast (e.g., Stark et al. 2015) typically depends on a constant contrast floor from the Inner Working Angle (IWA) to the Outer Working Angle (OWA). However, the sensitivity of coronagraphs varies as a function of radius from the star. In order to estimate the sensitivity of a coronagraphic telescope to exoplanets, we define contrast as the raw instrumental ratio of spurious speckle light to the peak of the stellar point-spread function (PSF).

The speckle brightness depends on the sum of the amplitudes of system wavefront errors at a particular spatial frequency (Traub & Oppenheimer 2010, their Equation (123)).

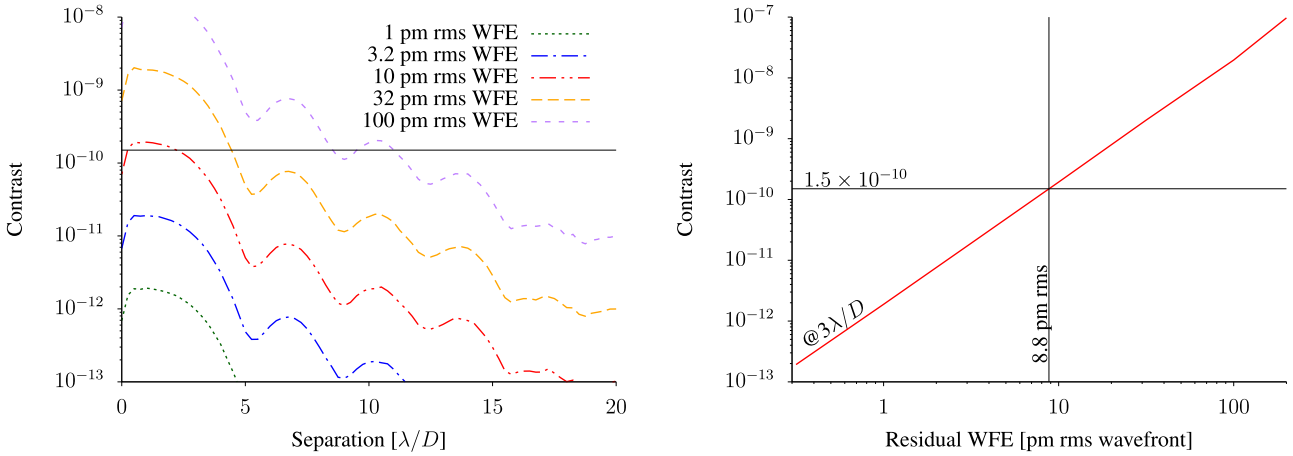

Figure 1. Left: numerical simulation of contrast vs. rms segment motion wavefront error for an ideal coronagraph. Curves show decreasing wavefront error from top to bottom. A horizontal line indicates the contrast of an Earth-radius exoplanet with an albedo of 0.25 at quadrature. Right: raw contrast vs. residual WFE at 3 λ/D, showing that 10 pm is a good approximation for a WFE requirement for detection of Earth-like planets with a segmented-aperture telescope.

In order to assess the influence of segment motion on speckle brightness, we developed a numerical model in the Fraunhofer diffraction regime of an ideal coronagraph (Males & Guyon 2018) and a segmented primary mirror. Contrast curves are shown in the left panel of Figure 1 for a variety of rms segment wavefront disturbances and compared to an Earthlike exoplanet contrast (horizontal line). The contrast as a function of angle peaks near $1\lambda/D$, where the low-spatial-frequency segment motion has the largest impact; 10 pm rms (dotted–dotted–dashed line) corresponds to a contrast of approximately 1.5×10^{-10}. Earthlike planet yield is highly sensitive to a coronagraph's IWA (Stark et al. 2015) and these low-spatial frequency errors likewise strongly impact sensitivity. These results are generally consistent with recent work on segmented mirror impact on coronagraph contrast (e.g., Ruane et al. 2017; Leboulleux et al. 2018), with the caveat that here the segment tip-tilt and piston modes have been normalized to contribute equal rms optical path difference (OPD) disturbances.

2.2. Wavefront Error Simulation

This section will explore the relationship between mechanical stability and incident photon rate by applying a control law to the PSD defining segment motion. This will lay the groundwork for setting design constraints on artificial laser guide stars. A realized optomechanical system will have time-dependent OPDs arising from a variety of mechanical disturbances (see Bronowicki 2006; Shi et al. 2016). To constrain the problem, we assume a smooth PSD. The form of the functional PSD we have chosen for modeling the longer timescale motion of primary mirror segments is similar to previous work, but with a few key differences. Previous work by Lyon & Clampin (2012) assumed an OPD PSD with respect to frequency, f, of the form:

$$\mathcal{T}(f) \propto \frac{1}{1 + \left(\frac{f}{f_n}\right)^{\alpha}}. \quad (1)$$

Here α is a power-law constant and f_n is the "knee frequency" where the distribution rolls off. A form commonly used to model optical surfaces (Church & Takacs 1986, 1991; Toebben et al. 1996; Harvey et al. 2009) is the K-correlation model, which in optical turbulence modeling is known as the von Karmàn PSD (Hardy 1998; Andrews & Philips 2005). We

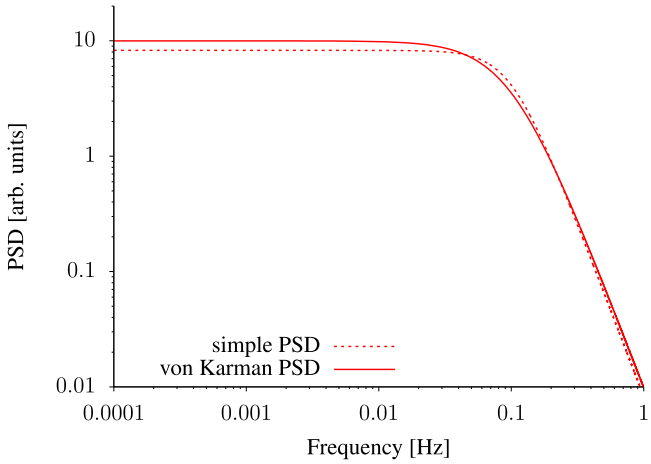

Figure 2. Comparison with arbitrary units of the simple PSD form of Equation (1) with the more general von Karmàn or K-correlation form of Equation (2). For equal knee frequencies, $f_n = 0.1$ Hz in this case, the forms are very similar. We adopt the von Karmàn PSD in this work.

adopt the following form as the PSD of the optical path difference due to segment motion:

$$\mathcal{T}_{\rm OPD}(f) = \frac{\beta^2_{\rm OPD}}{(f_o^2 + f^2)^{\alpha/2}}. \quad (2)$$

Here $\beta_{\rm OPD}$ is a normalization constant and f_o is the knee frequency, which is defined in terms of an "outer time" T_0 by $f_0 = 1/T_0$ (in analogy with the outer scale in turbulence). This has a slightly different form from that used by Lyon & Clampin (2012) for both spatial and temporal PSDs. Figure 2 directly compares the two similar forms. Here f_0 is essentially equivalent to their "drift frequency" f_n. In addition to its more general use in the literature, we prefer the PSD in Equation (2) to that Equation (1) due to its simpler behavior as $f_0 \to 0$, where it trivially becomes pure $1/f^{\alpha}$ noise.

Whether or not such PSDs are integrable depends on f_0 and α. In order to allow any value of these parameters, we adopt a band-limited stability specification. We call this σ_{10}, or the "rms in 10 minutes," i.e., "10 pm rms in 600 s." We normalize the PSD accordingly, from the frequency corresponding to 10 minutes to one-half of f_s, the sampling frequency of the

Table 2
System Parameters Assumed in Wavefront Sensing and Control Calculations

Parameter	Value	Notes
Telescope diameter	9.2 m	Feinberg et al. (2017)
Segment geometry	Hexagonal	Eisenhower et al. (2015)
Segment face-to-face width	1.15 m	LUVOIR A (Pueyo et al. 2017)
Zero-mag photon flux	9.1×10^9 photons s^{-1}	Vega-based, in Bessel *V*-band
System throughput, *Tp*	0.1	including detector QE
λ	500 nm	
Loop update rate	10 Hz	
Loop delay	1.5 msec	
Δf	1/3600	The PSDs model 1 hr periods
$n_{\rm pix}$	16/segment	
$\sigma_{\rm ron}$	0.3 e^-/pixel/frame	Typical EMCCD read noise

wavefront control system, i.e.,

$$\beta^2_{\rm OPD} = \frac{\sigma^2_{10}}{\int_{\frac{1}{600s}}^{f_s/2} (f_o^2 + f^2)^{-\alpha/2} df}. \quad (3)$$

The PSD of measurement noise is given by Males & Guyon (2018) as:

$$\mathcal{T}_p(f) = \frac{\beta_p^2}{F_\gamma \tau_{\rm wfs} + n_{\rm pix}\sigma^2_{\rm ron}} \left(\frac{\tau_{\rm wfs}}{2}\right), \quad (4)$$

where we are ignoring background noise sources that will not significantly impact the shape of the PSD; $n_{\rm pix}$ is the number of detector pixels used, each with readout noise $\sigma_{\rm ron}$. See Table 2 for assumed noise values and the number of pixels per segment. Since $\tau_{\rm wfs}$ appears in both the numerator and denominator, when $\sigma_{\rm ron}$ is set to zero the $\tau_{\rm wfs}$ cancels and for Equation (4) the measurement noise PSD does not depend on wavefront sensor exposure time, $\tau_{\rm wfs}$, given a noiseless (or low-noise) detector.[4]

The observed PSD depends on the measured system losses. For the current LUVOIR design, a system optical throughput to the wavefront sensor of 37.39% at 532 nm and 41.20% at 980 nm is expected (M. R. Bolcar 2018, private communication). We set a conservatively low throughput of 10% to account for reflective losses, as well as other terms decreasing the photon count rate, including the detector quantum efficiency, surface contamination and degradation, and aperture obscuration.

To understand the impact of wavefront sensing we select a Zernike wavefront sensor (ZWFS), which has ideal photon noise limited sensitivity across spatial frequencies (Guyon 2005) and is proposed for the baseline LUVOIR and the Habitable Exoplanet Observatory Mission Concept (HabEx) coronagraph designs (Pueyo et al. 2017; Gaudi et al. 2018). A ZWFS has been studied for cophasing large segmented-aperture space telescopes to the nanometer level (Janin-Potiron et al. 2017), and one is planned for low-order wavefront sensing in the Wide-Field InfrarRed Survey Telescope (WFIRST) coronagraph instrument (Shi et al. 2016). Alternatively, a pyramid wavefront sensor could provide autocalibration of intensity variation, at the expense of increased noise levels (Guyon 2005). The parameter β_p describes the sensitivity of the WFS to photon noise for the spatial frequency considered (Guyon 2005, Appendix A). For a ZWFS measuring rigid-body motion using photons striking a particular segment (Guyon 2005; N'Diaye et al. 2013),

$$\beta_p = \frac{1}{2}. \quad (5)$$

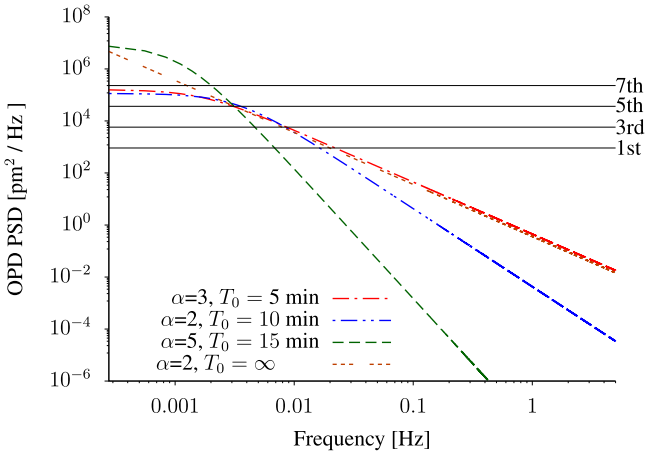

Figure 3. Comparison of PSDs with different power-law constants (α) and different T_0 outer times. The dashed lines show the optical path difference PSDs and the horizontal solid lines show the measurement noise floor for stars of different magnitudes. For $m_{\rm V} = 7$ and dimmer stars, measurement noise dominates. Even for a steep $\alpha = 5$ PSD, stellar noise will dominate above 0.01 Hz for an $m_{\rm V} = 1$ star. This sets the >100 s stability requirement for natural guide stars. All OPD PSDs are normalized with $\sigma_{10} = 10$ pm rms.

In Figure 3 we compare OPD PSDs with a range of α and T_0 values. This demonstrates that 0.01 Hz is the approximate sensing limit due to stellar photon noise per segment, even for bright stars (the stellar magnitude limiting photon noise is shown by horizontal solid lines). For this discussion, natural guide star wavefront sensing is limited to the photons solely within *V*-band (Bessell 2005) with the zero-magnitude flux listed in Table 2.

2.3. Closed-loop Wavefront Control

In order to assess how close the segment position can be controlled to the stellar sensing limits, we apply the framework developed in Males & Guyon (2018) for modeling the dynamics of a closed-loop control system. Given the two PSDs just described, $\mathcal{T}_{\rm OPD}(f)$ (Equation (2)) and $\mathcal{T}_p(f)$ (Equation (4)), the output PSD from a closed-loop control system is given by:

$$\mathcal{T}(f) = \mathcal{T}_{\rm OPD}(f)|{\rm ETF}(f)|^2 + \mathcal{T}_P(f)|{\rm NTF}(f)|^2, \quad (6)$$

where ETF(f) is the system Error Transfer Function and NTF (f) is the system Noise Transfer Function. These transfer functions describe the action of the control system on the input PSDs, and include the effects of finite integration time, a delay for calculation and communication, and the feedback control law. As expected from Equation (4), the OPD contribution of measurement noise is flat versus frequency, while the power-law constant (α) drives the slope of the OPD and T_0 sets the roll-off frequency. For the example cases where $\alpha = 2$ and $T_0 = 10$ minutes and $\alpha = 3$ and $T_0 = 5$, the OPD floor just barely exceeds the noise floor for a seventh magnitude star, so

[4] Conversely, note that the total measurement noise depends on the integral of the PSD, and thus depends on the exposure time.

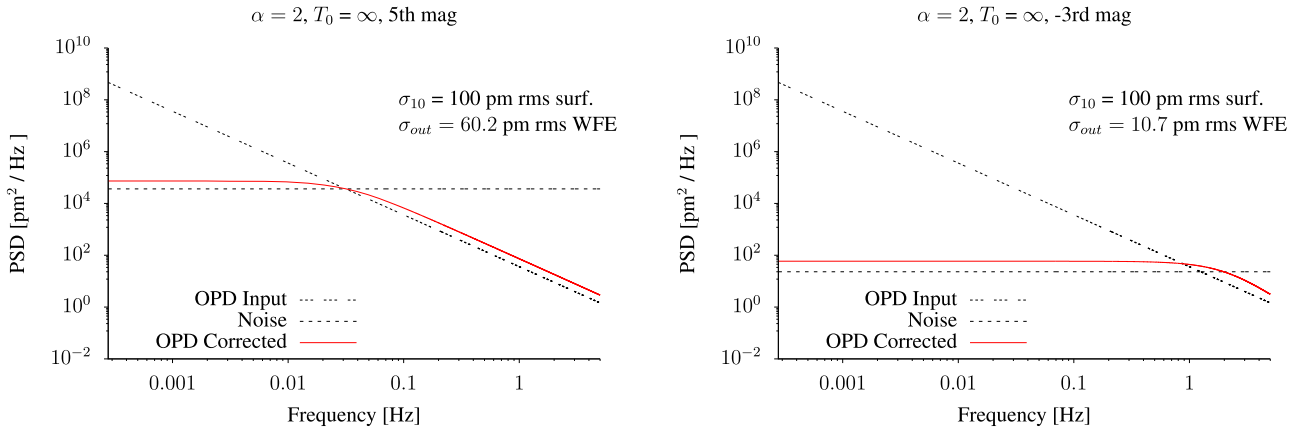

Figure 4. Example application of closed-loop control to OPD using $m_V = 5$ (left) and $m_V = -3$ (right) guide stars. The input disturbance is shown as a triple-dashed line and the corrected output is a solid line. The photon limited noise floor is shown as a horizontal dashed line.

wavefront control on stars dimmer than seventh magnitude would not benefit such a system.

3. Artificial Laser Guide Star Spacecraft Concept

Rather than guiding on a science star as assumed previously, one might use an artificial guide star to achieve an increased wavefront sensing flux. In order to maintain 10 pm stability, while observing dimmer stars, we explore the potential of a formation-flying spacecraft with a continuous-wave light source, providing more photons than a natural star. The geometry of the LGS concept is shown in Figure 6. The segmented space telescope with radius R_T is shown on the left. The LGS is shown at a distance z, projecting a Gaussian laser beam (to ensure smooth propagation) with a divergence, θ, at the telescope. While the telescope observes a target star at some astronomical coordinate, the LGS appears offset by some angle $d\alpha$. Table 2 includes several key parameters of the system that we will consider for the design trades throughout this work. Section 4 will describe the design constraints on an LGS for augmenting an Earth-like exoplanet coronagraph mission using typical telescope properties drawn from recent publications covering the design of the LUVOIR mission concept (Feinberg et al. 2017; Pueyo et al. 2017).

4. Results

4.1. Photon and Sensor Noise

The photon noise rate per segment places a limit on the sensing of the segment position. The closed-loop analysis of Section 2.3 relates guide star magnitude, natural or artificial, to residual wavefront error. Figure 4 shows that the input OPD is well-corrected to near the noise floor at low frequencies. The input disturbance is shown as a triple-dashed line and is suppressed in the controlled curve (solid line) by more than six orders of magnitude at low frequencies. Wavefront control could be implemented through direct control of segments via a hexapod (e.g., Contos et al. 2006), or a deformable mirror (two high-actuator count microelectromechanical systems—MEMS—deformable mirrors are planned for LUVOIR, Pueyo et al. 2017). The most important parameter is the overall level of vibrations, which we have characterized as the 10 minute rms, σ_{10}. The challenge of controlling these vibrations is shown in Figure 5 for the case of $\sigma_{10} = 10$ minutes and $\alpha = 2$ (left panel) and $\alpha = 3$ (right panel). For $\sigma_{10} = 10$ pm, a 10 pm residual OPD is achieved for an approximately second magnitude or brighter guide star. This would limit coronagraphy of a Sunlike stars to within just 3 parsecs for natural guide stars and sets a useful lower limit on the dimmest LGS for Earth-like exoplanet imaging. The only FGK stars that are this nearby and bright are Centauri A and Centauri B; however, as shown in Section 5.2, there are dozens of stars of interest that are of apparent magnitude greater than second and over 100 that are brighter than third magnitude or have other spectral types. To control much larger disturbances, such as $\sigma_{10} = 1$ nm residual OPD, a $m_V = -2$ or brighter guide star is needed.

4.2. Pointing Sensitivity

In addition to variations in the pupil plane intensity due to photon noise, changes in the guide star illumination pattern must also be considered in order to set the LGS performance requirements. Unlike the even illumination pattern of a natural guide star, the LGS beam will have a Gaussian intensity distribution. As discussed in Section 4.1, the ZWFS is sensitive to both intensity and phase variations. The ZWFS is effectively an interferometric fringe pattern at a single relative phase shift. Thus, intensity variations lead to spurious phase measurements. This is a concern for the LGS because the Gaussian laser beam will produce a variable illumination pattern across the observatory pupil, which moves according to the pointing of the LGS relative to the observatory ($d\alpha$ in Figure 6).

In addition to photon noise, if the pupil intensity function is changing on the timescale of segment jitter, due to changes in the pointing of the LGS, the WFS will sense erroneous tilts across the pupil. If the Gaussian function is static across the pupil, then it is straightforward to calibrate a static nonuniform intensity function. For example, Figure 7 shows a simple numerical model of a ZWFS generated using the Fresnel propagation environment in the Physical Optics Propagation in PYthon library (Perrin et al. 2016). A Gaussian intensity distribution (left panel), and a flat phase (middle panel) define the input wavefront. For simplicity and to maintain the optimal choice of mask diameter, the hexagonal aperture was truncated to a circumscribed circle for this simulation. After propagation to the image plane and multiplication by a complex phase mask with the optimal diameter (N'Diaye et al. 2013) of 1.06λ and $\theta = \pi/2$, propagation to the next pupil plane gives the measured pupil intensity shown in the right-hand panel of Figure 7. For small phase shifts ϕ, and an intensity I in a ZWFS

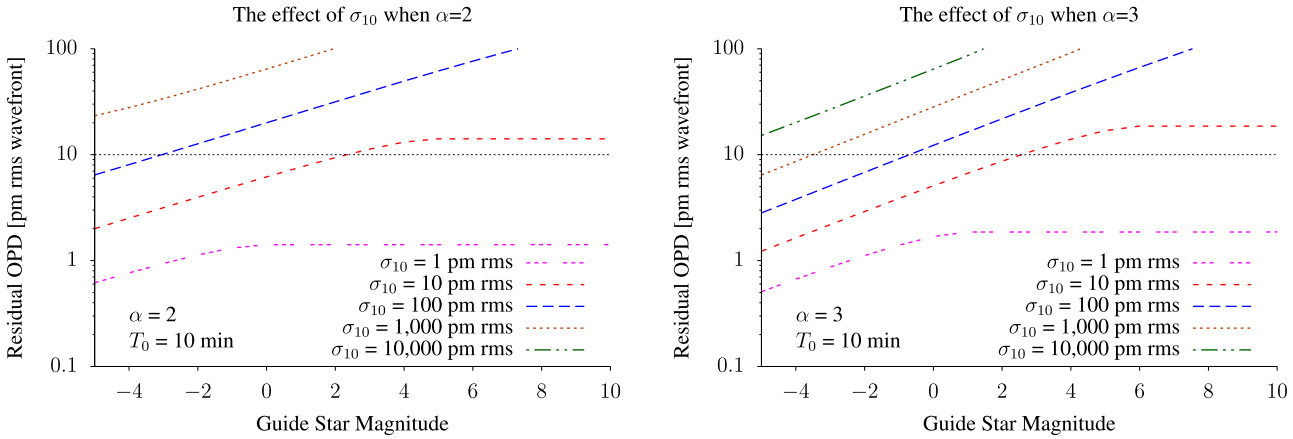

Figure 5. Residual segment disturbance OPD as a function of guide star magnitude for $\alpha = 2$ (left) and $\alpha = 3$ (right) for $T_0 = \infty$. The rms residual across all temporal frequencies, $\sigma_{\rm out}$, for the $m_{\rm V} = 5$ star is 60.2 pm, which is too high to detect Earthlike exoplanets. Conversely, a hypothetical $m_{\rm V} = -3$ guide star is sufficient to control OPD to 10.7 pm and reach contrasts of $\sim 10^{-10}$. These guide star magnitudes assume a 10% system throughput. For an ideal detector and minimal loss system with ∼40% throughput, these curves shift 1.5 magnitudes dimmer.

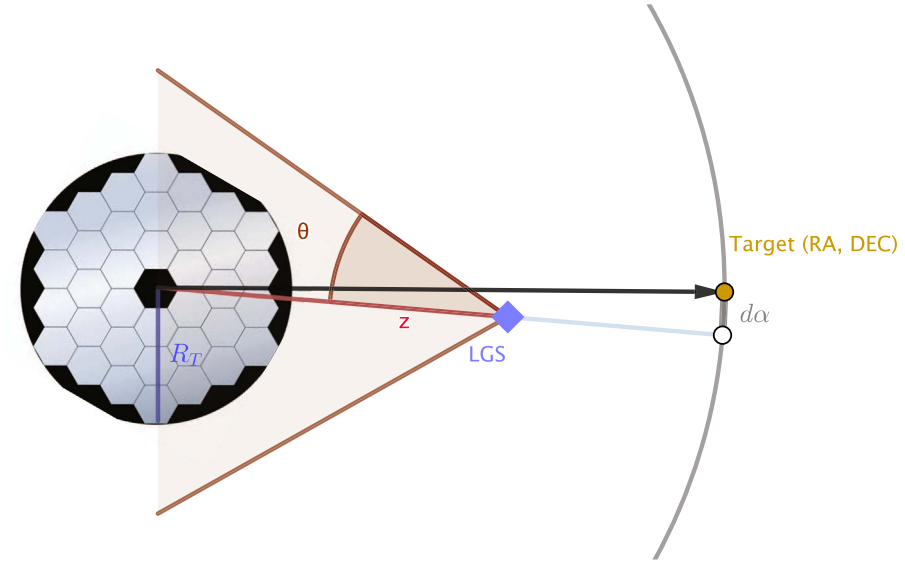

Figure 6. Two-dimensional representation of the LGS observing scenario. The observing telescope (left) direction of regard is shown as a vector projected onto the celestial sphere (right), while at range z the LGS (tilted square) is offset from the direction of regard by angle $d\alpha$. The width of the Gaussian LGS beam, with a half-width divergence θ, is shaded.

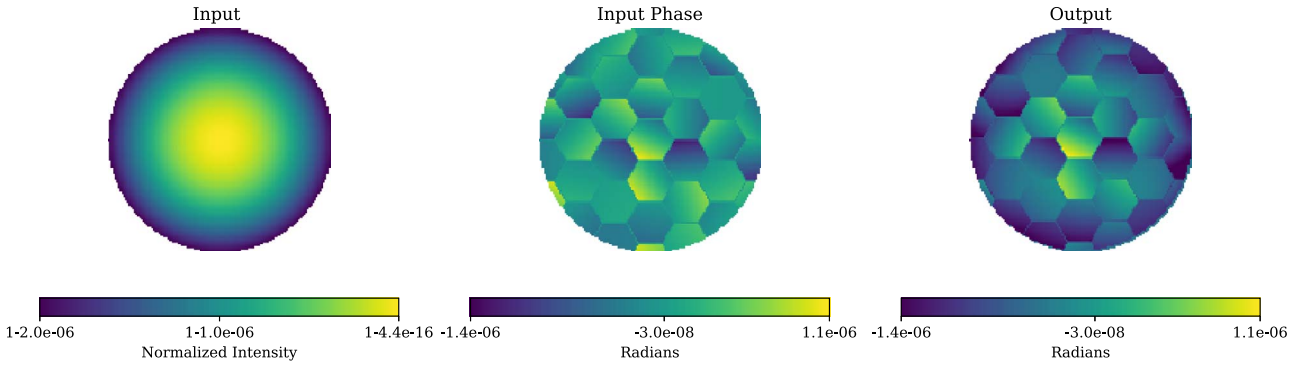

Figure 7. Example of ZWFS with an LGS, illustrating that a Gaussian input beam and a flat input phase disturbed by random segment motion (middle) leads to a varying output intensity (right) that is degenerate with phase errors. Accurate LGS pointing allows for quasi-static measurement of the intensity distribution and correction of this error. This simulation used $w = 23\farcs40$ at a range of 4.4×10^4 km, which corresponds to a beamwidth of 4.7 km at the telescope.

pixel, N'Diaye et al. (2013, Equation (15)) give the linear relation between phase and intensity as:

$$\phi = I/I_0 - 0.5. \tag{7}$$

I_0 is the average intensity across the pupil. Differentiating shows that the phase measurement error as a function of intensity error dI is:

$$d\phi = dI/I_0. \tag{8}$$

We quantify the pointing jitter error by calculating the fractional intensity difference between an on-axis LGS Gaussian beam striking the telescope I_1' and I_2', the same beam offset by x_0:

$$dI/I = \frac{I_1' - I_2'}{I_0} = e^{\frac{-2x^2}{w^2}} - e^{\frac{-2(x+x_0)^2}{w^2}}, \tag{9}$$

where x is the radial displacement from Gaussian beam, w is the beamwidth, and I_0 is the intensity. For $x = 0$, then $dI/I' = 1 - e^{\frac{-2x_0^2}{w^2}}$. The first-order Taylor expansion is:

$$d\phi \approx dI = 1 - \left(1 - \frac{2x_0^2}{w^2}\right) = \frac{2x_0^2}{w^2}. \tag{10}$$

Plugging in a minimum required phase error of 10 pm and a pointing error between measurements (e.g., 15 mas) allows us to solve for the minimum beamwidth w. Due to the need to stabilize intensity across the pupil, this gives a ratio of divergence versus transmitter jitter of >100, which is much larger than the typical values used to maximize received intensity for similar applications such as laser communications (e.g., ratio of divergence versus transmitter jitter of ~10, Clements et al. 2016). For LGS jitter of 15 mas, a level of performance regularly exceeded 3× by previous space observatories (e.g., Nurre et al. 1995; Koch et al. 2010; Mendillo et al. 2012), the divergence required to keep the jitter induced errors within 10 pm is >0.″325, limited by the (MFD) and allows more feasible laser powers. Regardless of the guide-star approach, for coronagraphic Earthlike planet imaging, the observatory pointing jitter must be much lower than that required for the LGS transmitter, well below 1 milliarcsecond, in order to maintain 10^{-10} contrasts (Ruane et al. 2017).

4.2.1. Beam Divergence Limitations

The finite size of a single-mode fiber generating the LGS beam and diffraction from the exit aperture further limit the minimum LGS beam divergence. The fiber mode-field diameter half-angle divergence is given by:

$$\theta_{\mathrm{MFD}} = \mathrm{MFD}/(2f) \tag{11}$$

where MFD is the mode-field diameter of the optical fiber and f is the focal length of the collimating optics. In addition to the mode-field diameter, the size of the exit aperture constrains the beam divergence. Likewise, for a Gaussian beam, the half-angle beam divergence is given by:

$$\theta_w = \lambda/(\pi w_0). \tag{12}$$

where w_0 is the beam waist (Kogelnik & Li 1966, Equation (22)). To minimize diffraction effects, we assume w_0 is one-third or less of the LGS exit aperture radius.

4.3. Wavelength Selection

The LGS may contribute background signal to science observations via scattered light, thermal emission, and fluorescence. A longer-than-science wavelength out-of-band laser source minimizes fluorescence and scattering internal to the telescope (e.g., via dichroic filters) while a high-efficiency laser minimizes waste heat. For simplicity, in this initial study, we will consider two common laser wavelengths, 980 nm and 532 nm. Longer wavelengths allow a decrease in the range between the LGS and telescope (Section 4.4), and a 980 nm source is within the sensitivity range of silicon detectors. Efficiency is also critical to designing a spacecraft with feasible thermal control, and 980 nm lasers have been previously shown to provide better than 50% wall-plug efficiency in continuous operation (Crump et al. 2005). Alternatively, the guide laser could be blocked by a narrow line-blocking interferometric filter. Contamination of high-contrast images by LGS light presents an additional consideration. Narrowband interferometric rejection filters with 8 orders of magnitude rejection in ultraviolet (UV) and visible wavelengths have been manufactured (Landulfo et al. 2018), and the LGS would be further suppressed by keeping the transmitter inside the coronagraph IWA (see Section 4.5). As described in Section 4.4, a shorter wavelength could provide a reference source closer to the center of the visible light science band (Pueyo et al. 2017).

4.4. LGS Formation Flying Range

Since the LGS is a finite distance from the telescope, we must account for the defocus of the reference wavefront. For a spherical wave emanating from the LGS at distance z (the range to the center of the entrance aperture), the peak-to-valley (PV) defocus is given by difference between z and R_C, the range to the edge of the aperture. Solving for R_C as a function of telescope aperture and the peak-to-valley wavefront error across the pupil $\mathrm{PV_{WFE}} = R_C - z$:

$$R_C = \frac{\mathrm{PV_{WFE}^2} + R_T^2}{2\mathrm{PV_{WFE}}} \approx \frac{R_T^2}{2\mathrm{PV_{WFE}}}, \tag{13}$$

for a telescope radius R_T. The quasi-linear range where Equation (7) holds for a ZWFS is approximately $\pm\pi/4$ (N'Diaye et al. 2013). Since $\sigma_{10} \ll \pm\pi/4$, for the configurations considered here, slight variations from nonlinearity are expected to be measurable for calibration. Hence, for PV wavefront error less than $\pi/2$,

$$R_C = 2R_T^2/\lambda. \tag{14}$$

Thus, the minimum range to the baseline telescope is 43,184 km at 980 nm. The addition of a defocusing mechanism in front of the wavefront sensor would relax this requirement, but may add noncommon path errors and tighten the lateral stability requirement discussed in Section 4.5.

4.5. LGS Position

This section will quantify the station keeping needed, or the accuracy with which the LGS must be held on the telescope-target-star vector during a coronagraphic exposure. Motion of the LGS across the sky relative to the target star will appear as a tilt to a telescope WFS. For the purpose of this study, we presume the telescope pointing is highly stabilized on board, such as by a Fine Guidance Sensor (FGS; Nurre et al. 1995), and that any bulk tilts across the wavefront sensor will be

Table 3
LGS Transmitter Design Parameters Possible Scenarios Where an LGS Illuminates a Segmented Telescope

Case	Telescope	Laser Power W	λ_{WFS} nm	z km	Throughput	θ $''$	Transmitter Jitter $''$	m	Band
I	Controlled	5.0	980.0	43184.0	0.1	3.861	0.015	−7.1	z'
II	Stable Telescope	0.005	980.0	43184.0	0.1	3.861	0.015	0.4	z'
III	Controlled	5.0	532.0	79549.0	0.1	3.861	0.015	−4.9	V
IV	Stable Telescope	0.005	532.0	79549.0	0.1	3.861	0.015	2.6	V
V	Controlled	5.0	980.0	43184.0	0.1	12.49	0.1	−4.5	z'
VI	Controlled	5.0	532.0	79549.0	0.1	12.49	0.1	−2.3	V

Note. The "stable" telescope cases, cases II and IV, are based on recent designs for a well-damped telescope using natural guide stars for wavefront sensing. The controlled cases, cases I, III, V, and VI, would use a more powerful laser to enable a faster update, relaxing telescope stability requirements. Throughput here refers to total observatory sensitivity, including the impacts of coating reflectivity and detector quantum efficiency. Transmitter jitter here is the maximum allowable excursion of the LGS beam from the boresight of the telescope. The rightmost "band" column indicates the filter over which the effective magnitude, m, is calculated.

subtracted. In order to enable effective tracking of the LGS, one might require it to hold position to within $0.25\lambda/D$ from the target star ($d\alpha$ in Figure 6). At the baseline range, this corresponds to a cross-track stability of 1 m, comparable to the requirements of starshade missions (e.g., Soto et al. 2017).

Such precise station keeping would also keep the LGS inside the coronagraph IWA, minimizing the contamination from light that leaks past any blocking filters (Section 4.3). Holding the LGS on the telescope boresight allows angular differential imaging (ADI) and keeps the wavefront tilt within the range of the ZWFS without an additional tip-tilt mirror in the wavefront sensing path, minimizing sensing of spurious off-axis aberrations.

Reflected sunlight from the LGS could contribute incoherent background to coronagraphic observations. For example, neglecting the solar panel reflectivity, given a 300 mm × 300 mm spacecraft cross-section, at the 5×10^4 km range with an an albedo of 0.01, the scattered light is $m_V = 16$. A carbon nanotube coated spacecraft could potentially lower the albedo to 0.001, bringing the scattered light to as low as $m_V = 19$ (Cartwright 2015). This scattered light further motivates keeping the LGS well within the inner working angle, as sources inside λ/D will be attenuated by many orders of magnitude by most coronagraph designs (e.g., N'Diaye et al. 2016; Trauger et al. 2016; Zimmerman et al. 2016) For example, a charge-6 Vector Vortex Coronagraph (VVC) coronagraph suppresses point sources at $0.25\lambda/D$ by ∼15 magnitudes Ruane et al. (2017), making even the brighter scattered light case dimmer than a typical Earthlike planet.

4.6. Other Considerations

The LUVOIR concept includes simultaneous observations in UV, visible, and infrared (IR) with one channel serving as the wavefront sensor (Pueyo et al. 2017). As with reflected sunlight, discussed in Section 4.5, thermal emission of the spacecraft may contribute a significant background if the source is not behind the coronagraph mask.

A variety of means are available to separate incoming light from the LGS from the science signal. Coronagraph designs, such as the WFIRST-Coronagraph Instrument (CGI) and the HabEx VVC use rejected starlight from a reflective focal plane mask at the center of the field to feed a ZWFS. Other designs use reflected light from the Lyot stop (Mendillo et al. 2015; Singh et al. 2015). For an LGS with precision station keeping (Section 4.5) both of these approaches, likely in conjunction with dichroic or notch-blocking filters in the science channel, allow separation of LGS light from the wavelengths and angles of interest. For LGS wavelengths shorter than the science wavelength, the magnitude of fluorescence from transmissive optics (Engel et al. 2003), and the potential for laser induced contamination of reflecting surfaces (Wagner et al. 2014) will require consideration. Fluorescence effects are dependent on material and wavelength. Thus, testing of materials and wavelength selection, along with consideration of a multiwavelength LGS transmitter, is expected to mitigate these effects.

In addition to intensity variations due to pointing jitter, understanding the phase stability of the LGS transmitter is critical to assessing feasibility of an LGS spacecraft. Global changes in the phase due to changes in the lasing wavelength are negligible since the LGS is providing a reference wavefront for corrections of relative errors on short timescales. Controlling for optical aberrations in a small spacecraft often requires challenging thermal and optical control; however, in this case large aberrations are tolerable. For a 10 m scale telescope, the observatory aperture cross-section is small relative to the range discussed previously, meaning the error incident on the telescope wavefront is a very small subsample of any internal LGS aberrations. For example, for the minimum θ and range in Table 3, the incident beam waist is 0.8 km and a change in the radius of curvature; i.e., due to focus error internal to the LGS being small. To quantify this effect, we consider that the ratio between the PV error across the telescope aperture and across the incident Gaussian beam waist w, at range z, is given by

$$\frac{z - \sqrt{z^2 - (D_t/2)^2}}{z - \sqrt{z^2 - w^2}} \sim 10^{-4}, \tag{15}$$

effectively minimizing 100 nm scale disturbances across the LGS wavefront to picometer scales at the telescope. Such "diffraction-limited" stability is well within the range of small satellite optical systems (e.g., Allan et al. 2018).

5. Discussion

There are two key benefits to the LGS approach: the ability to directly image dimmer target star systems, and decreasing the mechanical stability requirements on the telescope. Designs at opposite extremes of possible LGS transmitted power are shown in Table 3. Equation (14) sets the range for the mission concepts for two laser wavelengths, 532 and 980 nm. Both rely on an accurately pointed guide star to provide constant intensity calibration where the pupil intensity function is held constant throughout the observation. For example, a "well

controlled" 5 W LGS case uses a bright guide star which can be sampled quickly at hundreds of Hertz while a "stable" case assumes a relatively stable telescope (e.g., $\sigma_{10} = 10$ pm) requiring fewer photons per second for WFSing, is shown to compare science performance with and without the LGS. The magnitude values in V-band are directly comparable to the x-axis of Figure 5, allowing estimation of the residual OPD given a known input OPD PSD. For example, Case VI allows correction of a 1000 pm rms input OPD to 10 pm rms for $\alpha = 3$. z' magnitudes are given for the 980 nm LGS cases.

5.1. Controlled Case: Relaxed Telescope Stability

In addition to increasing the available discovery space, an LGS has the potential to drastically relax telescope stability requirements, potentially decreasing spacecraft mass and cost. Since the system control authority is no longer limited by photon noise, primary mirror segments can be actively held in position. For example, Figure 5 shows that, for $\alpha = 3$, a $m_V = -4$ or dimmer guide star (cases I, III, and V in Table 3) could provide 10 pm segment control for a $\sigma_{10} = 1$ nm input disturbance when $T_0 = 10$ minutes. This is more than two orders of magnitude of relaxation in telescope stability compared to performing wavefront sensing using photons from a $m_V = 5$ science target. Alternatively, a shorter T_0 could be controlled with a brighter LGS or a smaller σ_{10}.

5.2. Stable Case: Increased Discovery Space

It is illustrative to estimate how reducing wavefront sensing noise impacts science yield for a telescope built with sufficient segment stability to reach 10^{-10} contrasts around $m_V = 5$ stars.

A highly corrected telescope coupled with an LGS would open up a large population of nearby candidate host stars to greater than 10^{-10} contrast imaging with future space telescopes with a low-power $\lesssim$50 mW LGS transmitter. This scenario for 532 nm and 980 nm laser wavelengths is shown in cases II and IV in Table 3. These stars may not be ideal for uninformed searches due to the longer exposure times required, but if more rocky exoplanets are discovered by upcoming sub-1 m s^{-1} radial velocity surveys of stars as dim as $V = 12$ (e.g., Halverson et al. 2016), the capacity for high-contrast imaging of stars with low apparent magnitude will be valuable.

For a well stabilized telescope, the transmitter jitter requirement for the LGS could be relaxed from the 15 mas discussed in Section 4.2. Given the divergence and pointing constraints discussed in Section 4.2, Cases V and VI show that example systems with a relaxed transmitter jitter of 0.″1 and correspondingly increased θ still result in a guide star that is several magnitudes brighter than science targets, providing several magnitudes of margin on 10 pm segment rigid-body sensing.

Previous research has suggested that 10 minute stability at the 10 pm level is necessary for the detection of Earthlike planets around fifth to sixth magnitude stars (Stahl et al. 2013, 2015). The analysis presented here shows that the combination of a limiting magnitude of $m_V = 5$ to $m_V = 6$ and $\sigma_{10} = 10$ minutes may be overly optimistic. The ideal coronagraph model output shown in Figure 1 supports the previous finding that 10 pm control of segment motion is necessary to reach contrasts of 10^{-10} at the IWA. However, after accounting for system transmission, detector noise, and photon noise using a closed-loop control law, Figure 5 shows controlling segment rigid-body motion to this level requires guide star magnitudes $m_V < 3$.

Unfortunately, many promising, nearby, exoplanet host stars are dimmer than either third or fifth magnitude, particularly M-dwarf stars, which may host the majority of terrestrial planets (Dressing & Charbonneau 2015; Shields et al. 2016). While the habitable zone is still largely unconstrained (see the discussion in Seager 2013); we explore the flux ratio of a canonical Earth-radius planet ($R_\oplus$) at the Earth-equivalent insolation distance, r_{eei}. This flux ratio is given by

$$\zeta_\oplus = \frac{A\Theta(\alpha)R_\oplus^2}{r_{eei}^2}. \tag{16}$$

Figure 8 plots m_V versus $\zeta_\oplus$ using data from ExoCat-1 (Turnbull 2015), for planets at the Earth-equivalent insolation distance with geometric albedo $A = 0.2$ and a typical $\Theta = 1/\pi$ phase function value (Robinson et al. 2015). These targets can be broken into four quadrants around the canonical Earth–Sun value at 10 pc, indicated with an encircled cross just above 10^{-10} at slightly below $m_V = 5$. Below 10^{-10} are hotter stars with habitable zones at farther separations. Dimmer than fifth magnitude, the majority of target stars are cooler than the Sun with slightly larger $\zeta_\oplus$ values, but there is a significant population of Sunlike and hotter stars within 30 parsecs with lower $\zeta_\oplus$ values that will be particularly hard to access with natural guide star sensing. The right panel of Figure 8 shows the cumulative distribution versus m_V for the Research Consortium On Nearby Stars (RECONS)[5] nearest 100 stars, and the EXOCAT-1 catalog of promising exoplanet host stars (Turnbull 2015). There are 463 exoplanet candidate host stars with $m_V \leqslant 5$ within 30 pc in the ExoCat-1 catalog and more than four times as many stars if the limiting magnitude is instead extended to tenth magnitude. As can be seen from the shading of points in Figure 8, many of these dim stars are cooler than the Sun, with less stringent contrast requirements. There are hundreds more stars between fifth and eighth magnitude with comparable flux ratios to the Earth at 1 au from the Sun. For the more conservative $m_V < 3$ limit found here, there are only 142 target stars visible. An LGS allows recovery of the contrast needed to search the future mission target stars for Earthlike planets with a coronagraph. Alternatively, a telescope stability, σ_{10}, <10 pm or a stability outer time, T_O, >10 minutes is needed.

6. Summary

This paper is intended to serve as a starting point in the explorations of design space for an LGS to control segmented telescope motion. We have summarized the key design parameters, including inter-spacecraft range, source wavelength, station keeping, and laser transmitter jitter for a spacecraft formation flying along the direction of regard of a segmented-aperture coronagraphic space telescope to provide a bright reference wavefront. By applying a closed-loop transfer function to wavefront control of rigid-body motion for the nominal LUVOIR segment geometry, we derive a wavefront sensing limiting magnitude for detection of Earth-like planets of $m_V < 3$ with an ideal coronagraph, given 10 minute telescope stability. The LGS concept as described enables relaxation of telescope segment stability by up to two orders of

[5] http://www.recons.org/TOP100.posted.htm, last updated 2012 January 1.

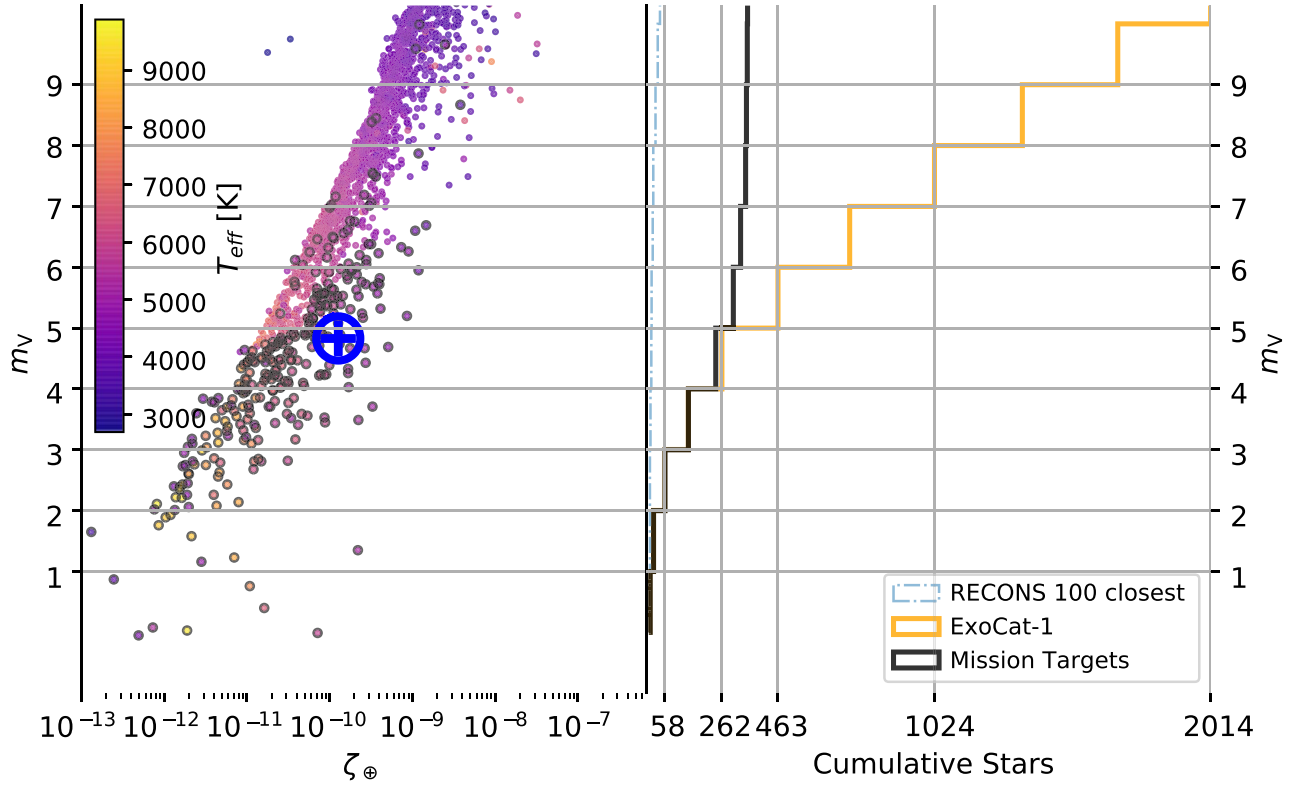

Figure 8. Left: magnitude vs. flux ratio of a $1R_\oplus$ planet at the Earth-equivalent insolation distance for stars in the ExoCat database below 10,000 K (Turnbull 2015). The Sun at 10 parsecs is shown as the encircled cross. Black outlined stars have been previously flagged by NASA missions as priorities for the WFIRST (Kasdin et al. 2018), Large Binocular Telescope Interferometer (LBTI; Ertel et al. 2018), Exo-S (Seager et al. 2015), and Exo-C (Stapelfeldt et al. 2015) projects in the Exoplanet Archive. Right: the cumulative number of target stars as a function of magnitude. There are 40 stars brighter than tenth magnitude in the RECONS databases of the closest stars and 2014 in ExoCat. Natural guide star wavefront sensing and 10 minute telescope stability place a limit at third magnitude or brighter, which leaves 142 ExoCat stars accessible. The solid black line shows the same mission stars as are circled in the left panel.

magnitude and offers the potential for nearly an order of magnitude increase in the number of stars observable to 10^{-10} raw contrast without wavefront sensing limitations.

This work will be followed by more detailed studies to optimize LGS feasibility and performance. Areas where further design studies are required include the number and lifetime of LGS spacecraft, range compensating wavefront sensor fore-optics, and alternative wavefront sensor architectures. In particular, laser wavelengths could be significantly shorter or longer; either increasing the sensitivity per photon or decreasing the wavefront curvature at a given range. Decreasing curvature would allow the LGS to fly closer and decrease maneuvering costs. It may be possible to trade these notional requirements for increased system complexity. For example, a focus and pointing correction stage could allow shorter LGS-telescope separations and relaxed station keeping requirements. Studies and laboratory simulations of the non-common-path ray propagation and higher-order diffraction effects of such solutions are presently underway (Y. Xin et al. 2018, in preparation, and Lumbres et al. 2018).

Large disturbances with steep power-law distributions, $\alpha > 3$, are readily correctable by an LGS of feasible brightness, which potentially enables relaxed segment positional stability requirements, decreasing the engineering changes relative to the structural design of the *James Webb Space Telescope* (*JWST*). Predictive control (Males & Guyon 2018) could also improve performance at resonance frequencies. For example, *JWST* has a 20 nm rms segment "rocking" mode at ~40 Hz (Stahl et al. 2015). The results above show that care must be taken to specify the full PSD envelope of OPD disturbances; otherwise, the actual limiting magnitude may be much brighter than expected.

The details of the LGS transmitter needed to provide precision pointing, particularly whether it is stabilized by a fine pointing system or body pointing, are the subject of future work along with development of control laws and quantification of the noise requirements for the attitude sensors and actuators.

Efforts are underway (captured in J. Clark et al. 2018, in preparation) to also develop mission architectures and spacecraft designs that optimize in terms of terrestrial planet yield while integrating state-of-the-art power, thermal, and propulsion technologies. These efforts include detailed operational restrictions due to reflections and orbital requirements at the Sun–Earth Lagrange Point 2 (L2). Coordination between multiple LGS in order to minimize delay between observations could significantly increase observing efficiency; a similar approach has been proposed for starshades, which have more complex systems with stringent requirements on fabrication, deployment, attitude, and navigation (Stark et al. 2016a).

This work was made possible by a NASA Early Stage Innovation Award, #NNX17AD07G. The team is grateful to Lee Feinberg and Ian Crossfield for many useful conversations. The authors would also like to thank the reviewer for many helpful comments. This research has made use of the NASA Exoplanet Archive,[6] which is operated by the California Institute of Technology, under contract with the National Aeronautics and

[6] Accessed 2018 July 16.

Space Administration under the Exoplanet Exploration Program. This research has made use of the SIMBAD database, operated at CDS, Strasbourg, France. This research has made use of data from RECONS (Henry et al. 2018). Figures related to ZWFS and yield calculations, as well as the numerical calculations in this work are available as a Jupyter notebook (Douglas 2018).

Facility: Exoplanet Archive.

Software: This research made use of community-developed core Python packages, including: Astroquery (Ginsburg et al. 2018), Astropy (The Astropy Collaboration et al. 2013), Matplotlib (Hunter 2007), SciPy (Jones et al. 2001), and the IPython Interactive Computing architecture (Pérez & Granger 2007).

ORCID iDs

E. S. Douglas https://orcid.org/0000-0002-0813-4308
J. R. Males https://orcid.org/0000-0002-2346-3441
J. Clark https://orcid.org/0000-0003-0615-2323
O. Guyon https://orcid.org/0000-0002-1097-9908
J. Lumbres https://orcid.org/0000-0002-3525-2262
W. Marlow https://orcid.org/0000-0001-9165-1180
K. L. Cahoy https://orcid.org/0000-0002-7791-5124

References

Allan, G., Douglas, E. S., Barnes, D., et al. 2018, Proc. SPIE, 10698, 1069857
Andrews, L. C., & Philips, R. L. 2005, Laser Beam Propagation through Random Media (2nd ed.; Bellingham, WA: SPIE Optical Engineering Press)
Basden, A., Brown, A. M., Chadwick, P., Clark, P., & Massey, R. 2018, MNRAS, 477, 2209
Beckers, J. M., Poland, C., Ulich, B. L., et al. 1982, Proc. SPIE, 0332, 42
Bessell, M. S. 2005, ARA&A, 43, 293
Bolcar, M. R. 2017, Proc. SPIE, 10398, 103980A
Bouchez, A. H., McLeod, B. A., Acton, D. S., et al. 2012, Proc. SPIE, 8447, 84473S
Bronowicki, A. J. 2006, JSpRo, 43, 45
Cartwright, J. 2015, PhyW, 28, 25
Church, E. L., & Takacs, P. Z. 1986, Proc. SPIE, 0645, 107
Church, E. L., & Takacs, P. Z. 1991, Proc. SPIE, 1530, 71
Clements, E., Aniceto, R., Barnes, D., et al. 2016, Proc. SPIE, 1116, 111610
Contos, A. R., Acton, D. S., Atcheson, P. D., et al. 2006, Proc. SPIE, 6265, 62650X
Crump, P., Wang, J., Crump, T., et al. 2005, Optimized Performance GaAs-Based Diode Lasers: Reliable 800-Nm 125W Bars and 83.5% Efficient 975-Nm Single Emitters, Tech. Rep. (Nlight Photonics Corp Vancouver WA)
Douglas, E. 2018, douglase/AJ_LGS_2018_PlotsAndFigs: updated figure 9 and added FITS OPD, Zenodo, doi:10.5281/zenodo.2529801
Dressing, C. D., & Charbonneau, D. 2015, ApJ, 807, 45
Eisenhower, M. J., Cohen, L. M., Feinberg, L. D., et al. 2015, Proc. SPIE, 9602, 96020A
Engel, A., Becker, H.-J., Sohr, O., Haspel, R., & Rupertus, V. 2003, Proc. SPIE, 5188, 182
Ertel, S., Defrère, D., Hinz, P., et al. 2018, arXiv:1803.11265
Feinberg, L., Bolcar, M., Knight, S., & Redding, D. C. 2017, Proc. SPIE, 10398, 103980E
Foy, R., & Labeyrie, A. 1985, A&A, 152, L29
Gaudi, B. S., Seager, S., Mennesson, B., et al. 2018, arXiv:1809.09674
Ginsburg, A., Sipocz, B., Parikh, M., et al. 2018, Astropy/Astroquery: V0.3.8 Release, Zenodo, doi:10.5281/zenodo.1234036
Gonte, F., Araujo, C., Bourtembourg, R., et al. 2008, Proc. SPIE, 7012, 70120Z
Greenaway, A. H., & Smith, D. M. 1990, ESAJ, 14, 169
Guyon, O. 2005, ApJ, 629, 592
Halverson, S., Terrien, R., Mahadevan, S., et al. 2016, arXiv:1607.05634
Hardy, J. W. 1998, Adaptive Optics for Astronomical Telescopes (Oxford: Oxford Univ. Press)
Harvey, J. E., Choi, N., Krywonos, A., & Marcen, J. G. 2009, Proc. SPIE, 7426, 74260I
Henry, T. J., Jao, W.-C., Winters, J. G., et al. 2018, AJ, 155, 265
Hicks, B. A., Jahoda, K., Petrone, P., Sheets, T., & Boyd, P. 2018, Proc. SPIE, 10698, 106986M
Holzlöhner, R., Rochester, S. M., Bonaccini Calia, D., et al. 2010, A&A, 510, A20
Hunter, J. D. 2007, CSE, 9, 90
Janin-Potiron, P., N'Diaye, M., Martinez, P., et al. 2017, A&A, 603, A23
Jared, R. C., Arthur, A. A., Andreae, S., et al. 1990, Proc. SPIE, 1236, 996
Jones, E., Oliphant, T., & Peterson, P. 2001, SciPy: Open source scientific tools for Python, http://www.scipy.org/
Kasdin, N. J., Turnbull, M., Macintosh, B., et al. 2018, Proc. SPIE, 10698, 106982H
Koch, D. G., Borucki, W. J., Basri, G., et al. 2010, ApJL, 713, L79
Kogelnik, H., & Li, T. 1966, ApOpt, 5, 1550
Landulfo, E., Guardani, R., Macedo, F. M., et al. 2018, Proc. SPIE, 10791, 107910B
Leboulleux, L., Sauvage, J.-F., Pueyo, L., et al. 2018, arXiv:1807.00870
Lumbres, J., Males, J., Douglas, E., et al. 2018, Proc. SPIE, 10703, 107034Z
Lyon, R. G., & Clampin, M. 2012, OptEn, 51, 011002
Macintosh, B., Troy, M., Doyon, R., et al. 2006, Proc. SPIE, 6272, 62720N
Males, J. R., & Guyon, O. 2018, JATIS, 4, 019001
Marlow, W. A., Carlton, A. K., Yoon, H., et al. 2017, JSpRo, 54, 621
Martinez, P., Janin-Potiron, P., Beaulieu, M., et al. 2018, Proc. SPIE, 10703, 1070357
Max, C. E., Olivier, S. S., Friedman, H. W., et al. 1997, Sci, 277, 1649
Mendillo, C. B., Brown, J., Martel, J., et al. 2015, Proc. SPIE, 9605, 960519
Mendillo, C. B., Chakrabarti, S., Cook, T. A., Hicks, B. A., & Lane, B. F. 2012, ApOpt, 51, 7069
Mier-Hicks, F., & Lozano, P. C. 2017, JGCD, 40, 642
Miller, K., Guyon, O., Codona, J., Knight, J., & Rodack, A. 2015, Proc. SPIE, 9605, 96052A
N'Diaye, M., Dohlen, K., Fusco, T., & Paul, B. 2013, A&A, 555, A94
N'Diaye, M., Soummer, R., Pueyo, L., et al. 2016, ApJ, 818, 163
Nurre, G. S., Sharkey, J. P., Nelson, J. D., & Bradley, A. J. 1995, JGCD, 18, 222
Pérez, F., & Granger, B. 2007, CSE, 9, 21
Perrin, M., Long, J., Douglas, E., et al. 2016, POPPY: Physical Optics Propagation in PYthon, Astrophysics Source Code Library, ascl:1602.018
Perrin, M. D., Sivaramakrishnan, A., Makidon, R. B., Oppenheimer, B. R., & Graham, J. R. 2003, ApJ, 596, 702
Postman, M., Argabright, V., Arnold, B., et al. 2009, arXiv:0904.0941
Pueyo, L., Zimmerman, N., Bolcar, M., et al. 2017, Proc. SPIE, 10398, 103980F
Racine, R., Walker, G. A. H., Nadeau, D., Doyon, R., & Marois, C. 1999, PASP, 111, 587
Robinson, T. D., Meadows, V. S., Crisp, D., et al. 2011, AsBio, 11, 393
Robinson, T. D., Stapelfeldt, K. R., & Marley, M. S. 2015, arXiv:1507.00777
Ruane, G., Mawet, D., Jewell, J., & Shaklan, S. 2017, Proc. SPIE, 10400, 104000J
Seager, S. 2013, Sci, 340, 577
Seager, S., Turnbull, M., Sparks, W., et al. 2015, Proc. SPIE, 9605, 96050W
Serabyn, E. 2000, Proc. SPIE, 4006, 328
Shi, F., Balasubramanian, K., Bartos, R., et al. 2016, Proc. SPIE, 9904, 990418
Shields, A. L., Ballard, S., & Johnson, J. A. 2016, PhR, 663, 1
Singh, G., Lozi, J., Guyon, O., et al. 2015, PASP, 127, 857
Smith, D. E., & Zuber, M. T. 2016, 2016 IEEE Metrology for Aerospace (New York: IEEE), doi:10.1109/MetroAeroSpace.2016.7573271
Soto, G., Sinha, A., Savransky, D., Delacroix, C., & Garrett, D. 2017, Proc. SPIE, 10400, 104001U
Stahl, H. P. & MSFC Advanced Concept Office 2016, Proc. SPIE, 227, 147.22
Stahl, H. P., Postman, M., & Smith, W. S. 2013, Proc. SPIE, 8860, 886006
Stahl, M. T., Shaklan, S. B., & Stahl, H. P. 2015, Proc. SPIE, 9605, 96050P
Stapelfeldt, K., Dekens, F. & EXO-C Science and Design Teams 2015, EXO-C Final Rep. CL#15-1197, Imaging Nearby Worlds (CL)
Stark, C. C., Cady, E. J., Clampin, M., et al. 2016b, Proc. SPIE, 9904, 99041U
Stark, C. C., Roberge, A., Mandell, A., et al. 2015, ApJ, 808, 149
Stark, C. C., Roberge, A., Mandell, A., & Robinson, T. D. 2014, ApJ, 795, 122
Stark, C. C., Shaklan, S. B., Lisman, P. D., et al. 2016a, JATIS, 2, 041204
The Astropy Collaboration, Robitaille, T. P., Tollerud, E. J., et al. 2013, A&A, 558, A33
Thompson, L. A., & Gardner, C. S. 1987, Natur, 328, 229
Toebben, H. H., Ringel, G. A., Kratz, F., & Schmitt, D.-R. 1996, Proc. SPIE, 2775, 240

Traub, W. A., & Oppenheimer, B. R. 2010, in Exoplanets, ed. S. Seager (Tucson, AZ: Univ. Arizona Press), 111
Trauger, J., Moody, D., Krist, J., & Gordon, B. 2016, JATIS, 2, 011013
Troy, M., Chanan, G., Michaels, S., et al. 2008, Proc. SPIE, 70120Y
Turnbull, M. C. 2015, arXiv:1510.01731
Turnbull, M. C., Traub, W. A., Jucks, K. W., et al. 2006, ApJ, 644, 551
Wagner, P., Schröder, H., & Riede, W. 2014, Proc. SPIE, 9237, 92372B
Wizinowich, P. L., Mignant, D. L., Bouchez, A. H., et al. 2006, PASP, 118, 297
Woolf, N. J., Smith, P. S., Traub, W. A., & Jucks, K. W. 2002, ApJ, 574, 430
Zimmerman, N. T., Eldorado Riggs, A. J., Jeremy Kasdin, N., Carlotti, A., & Vanderbei, R. J. 2016, JATIS, 2, 011012